

See discussions, stats, and author profiles for this publication at: <https://www.researchgate.net/publication/10726336>

Low-pressure diffusion equilibrium of electronegative complex plasmas

Article in *Physical Review E* · June 2003

DOI: 10.1103/PhysRevE.67.056408 · Source: PubMed

CITATIONS

60

READS

46

6 authors, including:



Kostya Ostrikov

Queensland University of Technology

669 PUBLICATIONS 17,774 CITATIONS

[SEE PROFILE](#)



Igor Denysenko

V. N. Karazin Kharkiv National University

89 PUBLICATIONS 1,120 CITATIONS

[SEE PROFILE](#)



Sergey Vladimirovich Vladimirov

The University of Sydney

401 PUBLICATIONS 7,053 CITATIONS

[SEE PROFILE](#)



Shuyan Xu

Nanyang Technological University

315 PUBLICATIONS 4,812 CITATIONS

[SEE PROFILE](#)

Some of the authors of this publication are also working on these related projects:



Electromagnetic wave propagation through magnetoactive plasma layers [View project](#)



Solid objects in plasma flows [View project](#)

Low-pressure diffusion equilibrium of electronegative complex plasmas

K. Ostrikov,^{1,2,*} I. B. Denysenko,^{1,†} S. V. Vladimirov,³ S. Xu,¹ H. Sugai,⁴ and M. Y. Yu^{5,‡}

¹*Plasma Sources and Applications Center, NIE, Nanyang Technological University, 1 Nanyang Walk, 637616, Singapore*

²*School of Chemistry, Physics and Earth Sciences, The Flinders University of South Australia, Adelaide SA 5001, Australia*

³*School of Physics, The University of Sydney, 2006 New South Wales, Australia*

⁴*Department of Electrical Engineering, Nagoya University, Nagoya 464-8603, Japan*

⁵*Theoretical Physics I, Ruhr University, D-44780 Bochum, Germany*

(Received 13 February 2003; published 27 May 2003)

A self-consistent fluid theory of complex electronegative colloidal plasmas in parallel-plate low-pressure discharge is presented. The self-organized low-pressure diffusion equilibrium is maintained through sources and sinks of electrons, positive and negative ions, in plasmas containing dust grains. It is shown that the colloidal dust grain subsystem strongly affects the stationary state of the discharge by dynamically modifying the electron temperature and particle creation and loss processes. The model accounts for ionization, ambipolar diffusion, electron and ion collection by the dusts, electron attachment, positive-ion–negative-ion recombination, and relevant elastic and inelastic collisions. The spatial profiles of electron and positive-ion–negative-ion number densities, electron temperature, and dust charge in electronegative SiH₄ discharges are obtained for different grain size, input power, neutral gas pressure, and rates of negative-ion creation and loss.

DOI: 10.1103/PhysRevE.67.056408

PACS number(s): 52.25.Vy, 52.35.Fp, 52.25.Kn

I. INTRODUCTION

Electronegative plasmas are widely used in microelectronic, optical, and other industries for manufacturing miniature circuit chips, optoelectronic, photonic, and microelectromechanical devices, synthesis of novel nanostructured and biocompatible materials, plasma enhanced chemical vapor deposition (PCVD) of multilayer functional coatings, environmental remediation, etc. [1–3]. Such electronegative plasmas are typical examples of multicomponent complex plasma systems containing electrons, neutrals, positive and negative ions, as well as charged nanometer or micrometer sized colloidal grains that appear as a result of chemical reaction in the gas or plasma-surface interaction, together with gas-phase polymerization or nucleation triggered by negative ions and/or precursor nanoparticles [4,5].

Notwithstanding the usual undesirable aspects of dust particles as contaminants in microelectronics manufacturing, recent advances in research and applications of complex plasmas have revealed a number of novel phenomena related to the plasma-grown nanometer-sized particles. For example, amorphous silicon films grown under grain generation and coagulation conditions [6] can lead to new optoelectronics properties. In particular, these films can attend better transport and stability properties compared to *a*-Si:H films grown by conventional PCVD methods [7–9].

On the other hand, the plasma-grown colloidal grains can significantly affect the local as well as the global discharge characteristics that are critical for the efficient deposition of quality thin films. Numerous results have indicated a direct

link between the fine dust grains, the electron temperature, and the quality of the PCVD fabricated silicon films. For example, experiments [10] on PCVD of *a*-Si:H show that high quality films are obtained with low dust density and low electron temperature. Due to complexities in the gas phase as well as surface reactions, plasmas loaded with charged dust particles also lead to difficulties in precise process control and predictability. Thus, more efficient engineering of the plasma composition and reactivity is a challenge for research in this area.

One way to solve the problem is to predict and control *in situ* the variations of the electron temperature in the discharge that can dynamically affect the rates of the plasma production and loss, including that of the negative-ion radicals responsible for initial dust nucleation and clustering in the ionized gas phase. For example, naturally grown or externally dispersed dust grains often elevate the electron temperature of the pristine plasma, resulting in a reduced rate of production (e.g., via electron attachment) of dust-precursor negative ions such as SiH₃[−] [5,11,12]. This process represents a self-organization of the complex plasma equilibrium in response to the source of the perturbation arising from growth of the fine grains in the gas-phase. Thus, to predict and control such multicomponent complex plasmas and their response to dust creation and growth are a challenge to modern plasma-assisted processing technology.

Various aspects of the dynamic self-organization of complex plasma systems have been investigated by several authors. Most of the existing works on complex plasmas are either limited to electropositive (electrons, positive ions, and dusts) complex plasmas including transport and stability phenomena [13–15] or dust growth in electronegative (e.g., silane based) discharges accompanied by electron temperature fluctuations [4,6,16–19]. Due to the rather large number of elementary processes of particle creation and loss, electronegative complex plasmas should be treated as self-consistent

*Email address: ostr0005@flinders.edu.au; kostrikov@nie.edu.sg

†Permanent address: School of Physics and Technology, Kharkiv National University, 4 Svobody Square, 61077 Kharkiv, Ukraine.

‡Corresponding author.

Email address: yu@tp1.ruhr-uni-bochum.de

thermodynamically open systems where the stationary states are dynamically sustained by various particle creation and loss (mostly via volume recombination) processes in the plasma bulk, on the walls, and on the dust grain surfaces [20,21]. This approach has recently been extended [22] to complex plasma systems with negative ions. It is shown that in order to be physically self-consistent, processes such as ionization, diffusion, electron attachment, negative-ion–positive-ion recombination, dust charge variation, and dissipation due to electron and ion elastic collisions with neutrals and fine particles, as well as charging collisions with the dusts, should be taken into consideration since they can have similar time rates.

However, modeling of *nonuniform* plasma equilibria and proper accounting of the major particle and power balance mechanisms in low-pressure electronegative dusty discharges still warrant further investigation. In fact, most of the existing models do not self-consistently include the reorganization process in the particle or plasma system arising from variation of the dust size, as well as the control and other parameters that can also directly affect the equilibrium state. In this paper, we use a model that allows nonuniform equilibrium states of electronegative complex plasmas and self-consistently accounts for the major particle and power balance mechanisms. The effects of electron temperature, the reaction rates, as well as the control parameters relevant to industrial nanofilm fabrication are investigated.

Existing approaches to dusty plasma theory are mostly limited to relatively low-density (with positive-ion number density $n_i \leq 10^9 \text{ cm}^{-3}$) capacitively coupled plasmas (CCPs) that are widely used for laboratory experiments with externally dispensed dust particles. However, these are no longer the benchmark plasma reactors for microelectronics manufacturing, and they have recently been replaced by higher-density ($n_i > 10^{10} \text{ cm}^{-3}$) inductively coupled plasmas (ICPs) with lower near-substrate dc potentials and hence weaker dust grain trapping capacity. The risk of compromising the semiconductor film quality by uncontrollable fallout of gas-phase grown nanoparticles is thus increased. Therefore, a detailed study of electronegative complex plasmas at high densities is warranted.

In this paper, we use a theoretical model for high-density silane (SiH_4) plasmas in the parallel-plate geometry by considering a simplified species composition that can easily be extended to other silane based discharges. The choice of the neutral gas feedstock is based on the following reasons. First, low-pressure rf discharges in silane or mixtures of silane with other gases are used intensively today for the fabrication of modern silicon based thin-film devices such as transistors and solar cells. Second, the silane plasma is a classical fine grain generating plasma very often used in manufacturing as well as in the laboratory. Third, silane based plasma chemistries are relatively well understood and most of the required rate coefficients are readily available. The theoretical model is applied to study the characteristics of a high-density ($n_i > 10^{10} \text{ cm}^{-3}$) electronegative silane discharge and numerical results obtained. It should be emphasized that the model can be straightforwardly extended to other reactive plasmas with fine grains, including hydrocarbon [23]

and fluorocarbon [24] based powder-generating systems. The computations are carried out for pressure ranges and sizes of typical parallel-plate plasma reactors used in experiments on fine powder generation [16]. In particular, we investigate the effect of dust size variation and the dependence of the equilibrium structure on the external control parameters (input power and neutral gas pressure), creation and loss of negative ions, electron temperature, electron and ion number densities, as well as the grain charge. Conditions for efficient electron temperature control and the major reaction rate coefficients are obtained. It is shown that the equilibrium states of electronegative complex plasmas are quite different from their dust-free counterparts. Our model invokes three fluid equations for the electrons and two for the positive and negative ions. The charge on the colloidal nanograins is obtained from the conventional orbit motion limited (OML) approach.

The paper is organized as follows. The governing assumptions, equations, and boundary conditions of the multicomponent fluid model for electronegative plasmas are given in Sec. II. Analyses of the ambipolar electric field and particle fluxes in the low-pressure diffusion equilibrium are presented in Sec. III. The numerical model for the silane discharge is given in Sec. IV. Sections V and VI consider the effect of the external control parameters (input power and neutral gas pressure) on the equilibrium discharge states. The effect of the size and number density of the dusts on the spatial profiles of the main discharge parameters is investigated in Sec. VII. In Sec. VIII, the effect of negative-ion creation or loss on the electron temperature and particle densities is studied. Our results and their applications, as well as suggestions on possible improvements of the model, are discussed in Secs. IX and X. A brief summary of this work and outlook for future research are given in Sec. XI.

II. FORMULATION

For simplicity, we consider a one-dimensional (1D) parallel-plate discharge geometry. The discharge is symmetrical with respect to the midplane $x=0$ and bounded at $x = \pm L/2$ by metal or dielectric walls (Fig. 1). The electric field sustaining the discharge is uniform along the x direction. The electronegative plasma is composed of electrons, singly charged positive and negative ions, and negatively charged colloidal dust grains. It is assumed that size dispersion of the dust grains is negligible. The distribution of the colloidal particles in the discharge volume is chosen to fit the two most typically found grain profiles in the experiments. The first distribution, uniform along x , of the dust number density n_d (curve *a* in Fig. 1) is typical for particulate growth experiments using silane based gas mixtures [16]. The second profile (curve *b* in Fig. 1) reflects dust clouds formed in the vicinity of discharge walls and electrodes. Relevance of these profiles to laboratory complex plasmas will be discussed in Secs. IV and IX. The near-wall boundary conditions for the electron-ion fluxes and electron heat flows will be further discussed at the end of this section. Furthermore, we assume that $\tau_d \gg \tau_{eq}$, where τ_d and τ_{eq} are the characteristic time scales of grain motion and establishment of the

TABLE I. The main plasma and dust parameters used in the computations. The (singly charged) positive and negative ions are SiH_3^+ and SiH_3^- , respectively. The values of T_e , n_e , n_i , and n_- are that at the discharge midplane $x=0$.

Parameter	Notation	Value
Plasma slab width	L	3, 10 cm
Unit-area power input	P_{in}	0.12, 0.24, 1.2 W/cm ²
Electron density	$n_e(0)$	$5.6 \times 10^9 - 1.2 \times 10^{11} \text{ cm}^{-3}$
Electron temperature	$T_e(0)$	1.2–2.0 eV
Positive-ion density	$n_i(0)$	$3 \times 10^{10} - 1.7 \times 10^{11} \text{ cm}^{-3}$
Positive-ion temperature	T_+	0.035 eV
Positive-ion mass	m_+	$1836 \times 31 m_e$
Negative-ion density	$n_-(0)$	$10^{10} - 1.5 \times 10^{11} \text{ cm}^{-3}$
Negative-ion temperature	T_-	0.035 eV
Negative-ion mass	m_-	$1836 \times 31 m_e$
Dust density	n_d	$0.1 - 5 \times 10^7 \text{ cm}^{-3}$
Dust radius	a_d	50, 100, 200 nm
Neutral gas pressure	p_0	10, 100, 200 mTorr
Temperature of neutrals	T_n	0.035 eV

equilibrium state, respectively. Thus, the massive (compared to the other plasma particles) dust grains can be treated as immobile point masses. It is also assumed that $r_{Di} \ll d$, where r_{Di} is the ion Debye length (which can be approximately taken as the characteristic size of the sheath of a grain) and d is the interparticle spacing.

In the fluid approximation for the multicomponent plasma, we have the following particle balance equations:

$$\partial_t n_e + \partial_x \Gamma_e = \nu^i n_e - \nu_{\text{att}} n_e - \nu_{ed} n_e \quad (1)$$

for the electrons,

$$\partial_t n_i + \partial_x \Gamma_i = \nu^i n_e - K_{\text{rec}} n_i n_- - \nu_{id} n_i \quad (2)$$

for the positive ions, and

$$\partial_t n_- + \partial_x \Gamma_- = \nu_{\text{att}} n_e - K_{\text{rec}} n_i n_- - \nu_{-d} n_- \quad (3)$$

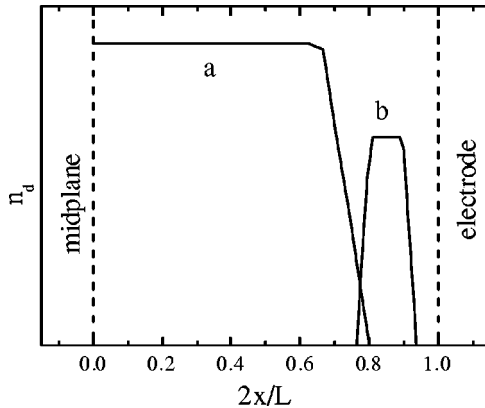


FIG. 1. Schematic diagram of the spatial profiles of n_d used in the computations. Curve a models a uniform dust distribution, and curve b corresponds to a dust cloud confined near an electrode. Here, $x=0$ corresponds to the discharge midplane.

for the negative ions, respectively. Here, n_α and Γ_α , where the subscripts $\alpha=e, i$, and $-$ stand for electrons, positive, and negative ions, respectively, is the density and flux of the plasma species α , ν^i , K_{rec} , and ν_{att} are the ionization, positive-negative ion recombination, and electron attachment rates, respectively, ν_{ed} , ν_{id} , and ν_{-d} are the rates of collisions of electrons, positive ions, and negative ions with the colloidal grains, respectively. It is further assumed that all the charged particles obey the Maxwellian energy distribution. Furthermore, the temperatures of the ions and neutrals are fixed at 400 K, which is typical for laboratory and industrial silane based plasmas containing dust grains [6]. In the ambipolar diffusion model, the fluxes of the charged particles in Eqs. (1)–(3) are given by [3]

$$\Gamma_e = -D_e \partial_x n_e - n_e \mu_e E,$$

$$\Gamma_i = -D_i \partial_x n_i + n_i \mu_i E, \quad (4)$$

$$\Gamma_- = -D_- \partial_x n_- - n_- \mu_- E,$$

where E is the ambipolar electric field, $D_\alpha = T_\alpha / m_\alpha \nu_{\alpha n}$ and $\mu_\alpha = |q| D_\alpha / T_\alpha$ are the diffusion and mobility coefficients, respectively. Here, $\nu_{\alpha n}$ are the effective rates of collisions (for momentum transfer) of species α with the neutrals [25]. The model assumes the overall plasma charge neutrality

$$n_i = n_e + n_- + n_d |Z_d| \quad (5)$$

and balance of the positive and negative particle fluxes,

$$\Gamma_i = \Gamma_e + \Gamma_-, \quad (6)$$

where Z_d is the dust charge.

The microscopic electron I_e , positive-ion I_i , and negative-ion I_- currents flowing onto a dust grain of radius a_d within the OML probe theory are [26,27]

$$\begin{aligned}
I_e &= -\pi a_d^2 e (8T_e / \pi m_e)^{1/2} n_e \exp(-e^2 |Z_d| / a_d T_e), \\
I_i &= \pi a_d^2 e n_i V_i (1 + 2e^2 |Z_d| / a_d m_i V_i^2), \\
I_- &= -\pi a_d^2 e n_- V_- \exp(-e^2 |Z_d| / a_d T_-),
\end{aligned} \tag{7}$$

where T_α , m_α , and $v_\alpha = \Gamma_\alpha / n_\alpha$ are the temperature, mass, and drift velocity of the species α , respectively, and $V_\alpha = (8T_\alpha / \pi m_\alpha + v_\alpha^2)^{1/2}$. In the steady state, the balance of the microscopic grain currents of the positive and negative plasma particles,

$$I_i + I_e + I_- = 0 \tag{8}$$

yields the equilibrium value of the dust charge. We note that in Eq. (8) the contribution of the negative ion grain current is usually small ($I_- \ll I_e$) in typical cold-ion ($T_- \ll T_e$) low-temperature plasmas.

The energy equation is given by [25]

$$\frac{3}{2} n_e \partial_t T_e + \partial_x q_e \approx -n_e J_e + S_{\text{ext}}, \tag{9}$$

where $q_e \approx -(5n_e T_e / 2m_e \nu_{en}) \partial_x T_e$ is the heat flux density, and

$$J_e = \sum_j \nu_j \mathcal{E}_j \tag{10}$$

is the electron collision integral. Here, ν_j is the effective rate of electron collisions with other particles and \mathcal{E}_j is the energy loss in the collisions. Usually, energy lost to the electron-neutral collisions is dominant.

When the plasma electrons are heated by rf fields, the Joule heating term S_{ext} in Eq. (9) is given by [25]

$$S_{\text{ext}} \approx n_e \nu_{en} m_e u_{\text{osc}}^2,$$

where u_{osc} is the time-averaged oscillation velocity of the electrons in an rf field. We shall assume that the rf field is uniform across the plasma slab. It is thus reasonable to expect that the electron temperature is also spatially uniform. However, a drop in T_e will occur near a plasma edge due to finite electron heat flow to the wall [28]. The equilibrium state of the discharge corresponds to setting $\partial_t = 0$ in all the equations. The rf power absorbed per unit area,

$$P_{\text{in}} = \int_{-L/2}^{L/2} S_{\text{ext}} dx,$$

is fixed in our computations.

We now consider the boundary conditions for integrating Eqs. (1)–(3), and (9). Because of the discharge symmetry, the gradients of the electron temperature and electron and ion number densities must vanish at $x=0$. At the slab edges ($x = \pm L/2$), we assume that the plasma flow follows the Bohm speed $u_B = \sqrt{T_e(\pm L/2) n_i / m_i n_e}$ [3]. The boundary condition [29] for the electron heat flow is

$$q_e = T_e (2 + \ln \sqrt{m_i / m_e}) n_e \sqrt{T_e / m_i},$$

where q_e , T_e , and n_e are evaluated at $x = \pm L/2$. Since usually $T_- \ll T_e$, the negative-ion flow to the negatively biased wall is generally small compared to that of the electrons [27] and can thus be neglected.

III. DIFFUSION EQUILIBRIUM

In the low-pressure diffusion equilibrium approximation, one obtains from Eqs. (4) and (6) the following expression for the ambipolar electric field and the electron and positive-ion fluxes:

$$E = (D_i \partial_x n_i - D_e \partial_x n_e - D_- \partial_x n_-) \xi^{-1}, \tag{11}$$

$$\begin{aligned}
\Gamma_e &= -(\mu_i n_i + \mu_- n_-) D_e \xi^{-1} \partial_x n_e - \mu_e n_e (D_i \partial_x n_i \\
&\quad - D_- \partial_x n_-) \xi^{-1},
\end{aligned} \tag{12}$$

$$\begin{aligned}
\Gamma_i &= -(\mu_e n_e + \mu_- n_-) D_i \xi^{-1} \partial_x n_i - \mu_i n_i (D_e \partial_x n_e \\
&\quad + D_- \partial_x n_-) \xi^{-1},
\end{aligned} \tag{13}$$

where $\xi = \mu_i n_i + \mu_e n_e + \mu_- n_-$. The ambipolar electric field (11) accelerates the positive ions and decelerates negative ions and electrons, so that there is a balance of the total particle flux (6).

Taking into account the overall charge neutrality (5), from Eqs. (12) and (13) we obtain

$$\begin{aligned}
\Gamma_e &= -[\mu_i n_i + \mu_- (n_i - n_e - n_d |Z_d|)] D_e \xi^{-1} \partial_x n_e \\
&\quad - \mu_e n_e (D_i \partial_x n_i - \chi D_-) \xi^{-1},
\end{aligned} \tag{14}$$

$$\begin{aligned}
\Gamma_i &= -[\mu_e n_e + \mu_- (n_i - n_e - n_d |Z_d|)] D_i \xi^{-1} \partial_x n_i \\
&\quad - \mu_i n_i (D_e \partial_x n_e + \chi D_-) \xi^{-1},
\end{aligned} \tag{15}$$

where $\zeta = (\mu_i + \mu_-) n_i + (\mu_e - \mu_-) n_e - \mu_- n_d |Z_d|$, and $\chi = \partial_x n_i - \partial_x n_e - \partial_x (n_d |Z_d|)$.

Using Eq. (5), one can eliminate n_- from the positive-ion conservation equation (2) to obtain

$$\partial_t n_i + \partial_x \Gamma_i = \nu^i n_e - K_{\text{rec}} n_i (n_i - n_e - n_d |Z_d|) - \nu_{id} n_i, \tag{16}$$

which will be used in the numerical analysis.

In the equilibrium state, when the fluxes of the positive and negative particles are balanced, from Eqs. (1)–(3) and taking into account Eq. (6), one can obtain

$$\nu_{ed} n_e + \nu_{-d} n_- = \nu_{id} n_i, \tag{17}$$

which is a fundamental relation between the number densities of the electrons and the positive and negative ions. The rates ν_{jd} ($j = e, i, -$) of plasma particle collection by the dust grain clearly plays an important role in determining the low-pressure diffusion equilibrium in the electronegative complex plasma.

In a complex plasma without negative ions, Eq. (17) is reduced to $n_e / n_i = \nu_{id} / \nu_{ed}$ [30], which shows that the number densities of the electrons and ions are inversely proportional to their rates of capture by the dust grains. In a chemically active complex plasma with enhanced negative-ion

density (often exceeding n_e [4]) the contribution of the negative ions to Eq. (17) is not negligible despite the relatively low negative-ion collection (by the dust grain) rate [27].

Following Eq. (12) of Ref. [31] and taking into account that $|I_i| \approx |I_e|$ [27], we obtain

$$\nu_{ed} = \pi a_d^2 n_d (n_i/n_e) V_i (1 + 2e^2 |Z_d|/a_d m_i V_i^2) \quad (18)$$

for the rate of the electron collection by the dust grains. In principle, the balance of the fluxes in the discharge should also involve the dust component. However, for the time scales of interest consistent with our model the heavy colloidal dust grains can be assumed to be stationary and uniformly distributed.

We note that Eqs. (11)–(15) for multicomponent electronegative complex plasmas also generalize a number of simpler cases. For example, in the absence of dust grains, Eq. (15) is simplified to Eq. (10.3.4) of Ref. [3]. If the negative-ion density is sufficiently high, the ion flux (15) becomes [3] $\Gamma_i \approx -[2T_i/(m_i \nu_{in})] \partial_x n_i$, where ν_{in} is the ion-neutral collision frequency. On the other hand, when the plasma contains only positive ions and electrons, Eqs. (14) and (15) are reduced to [3] $\Gamma_e = \Gamma_i \approx -[T_e/(m_i \nu_{in})] \partial_x n_i$.

Enhancement of the electron temperature is a common feature in many dust contaminated plasmas. In fact, T_e increases with the dust size and number density [6]. Because a large proportion of the total negative charge in the plasma resides on dusts and negative ions, the density of the positive ions is usually much higher than that of the electrons. One of the objectives of the present work is to predict the equilibrium states of complex electronegative plasmas resulting from a dynamic balance of the many elementary processes including electron-impact ionization, excitation, attachment to neutrals, positive-ion–negative-ion recombination, etc. It is found that the colloidal dust grains can significantly affect the electron temperature and thus the rates of most physical processes in the system, such as electron and ion production and destruction, and therefore also the efficiency of the desired applications.

In the following, we shall numerically study a specific complex discharge plasma at various conditions relevant to many modern applications. We note that most of the equations involved are strongly nonlinear and thus require rather rigorous numerical routines [28,32].

IV. NUMERICAL EVALUATION

In the numerical calculation we consider a typical complex silane discharge containing electrons, SiH_3^+ positive ions, SiH_3^- negative ions, and dusts. This choice allows us to make use of existing data on silane based discharges with the highest number densities of SiH_3^\pm ions [33]. A somewhat simplified species composition is used here for the sake of better transparency of the low-pressure diffusion equilibrium. The model can nevertheless be straightforwardly extended to plasmas with larger numbers of charged and neutral species.

We shall mainly consider plasmas with nearly uniform dust density profiles as given by curve *a* in Fig. 1. Such dust

distributions have been confirmed by the laser scattering techniques ≈ 20 –40 sec after the discharge startup (for example, see Fig. 4 of Ref. [16]). The size (50–200 nm) and number densities $[(0.1\text{--}5) \times 10^7 \text{ cm}^{-3}]$ of the dust grains adopted here are also typical for experiments. For example, the average grain size is ≈ 70 and 100 nm at 20 and 40 sec into a discharge run, respectively [16], and the concentration of 100-nm grains is estimated to be about 10^7 – 10^8 cm^{-3} [16]. We shall also consider the case where the dust grains are located at the discharge periphery. The corresponding profile as given by curve *b* in Fig. 1 reflects a frequent formation of dust clouds in the vicinity of the discharge walls [34].

The details of our numerical procedures can be found elsewhere [32,28]. The profiles of the electron and ion densities and velocities, and electron temperature are computed from Eqs. (1), (9), and (14)–(16). The computation is initialized using profiles of $n_{i,e}$, $\Gamma_{i,e}$, and T_e estimated from less accurate analytical or computational results. Basically, the time-dependent conservation equations are integrated and iterated until the desired steady state is reached as a result of the time evolution of the system. In this approach the highly nonlinear partial differential equations involved here are effectively replaced by linear ones and the self-consistent asymptotic (time-independent) solutions represent the steady or equilibrium states [28].

The electron-neutral collision rates in Eq. (1), (9), and (16) are determined using the cross sections for electron-neutral collisions in a silane plasma assuming the Maxwellian electron energy distribution. The cross sections and thresholds for vibrational excitation of the silane molecules, electron attachment, electron-impact excitation, ionization, and momentum transfer are taken from Figs. 2–4 of Ref. [35]. Different values of the ion-ion recombination coefficient are used in the computations: $K_{\text{rec}} = 5.0 \times 10^{-7} \text{ cm}^3/\text{s}$ [36], $2.0 \times 10^{-7} \text{ cm}^3/\text{s}$ [6], and $10^{-8} \text{ cm}^3/\text{s}$. The cross section for ion-neutral collisions is $\sigma_{in} = 6.0 \times 10^{-15} \text{ cm}^2$ [37]. The ion-neutral collision rate is then determined from $\nu_{in} = \sigma_{in} n_n V_i$, where n_n is the density of the neutrals. (See Table I.)

We now examine in detail the effects of the discharge operating parameters on the equilibrium states of the complex electronegative silane discharge plasma. The spatial distributions of the plasma parameters (densities of the electrons and positive and negative ions, the dust charge, and the electron temperature) are computed for different powers P_{in} absorbed per unit area in the discharge, and the neutral gas pressures p_0 . The equilibrium states are then compared to those of dust-free plasmas with negative ions.

V. EFFECT OF THE INPUT POWER

First, we shall consider the effect of input power variation. We take the width of the plasma slab $L = 3 \text{ cm}$, the silane gas pressure 100 mTorr, and the recombination coefficient $K_{\text{rec}} = 2 \times 10^{-7} \text{ cm}^3/\text{s}$. It is also assumed that the dust density is uniform with $n_d = 2 \times 10^7 \text{ cm}^{-3}$ for $x \leq 1 \text{ cm}$ and drops linearly to zero at $x = 1.25 \text{ cm}$ [curve *a* in Fig. 1]. This distribution implies a uniform dust production in the entire volume of the silane plasma [4].

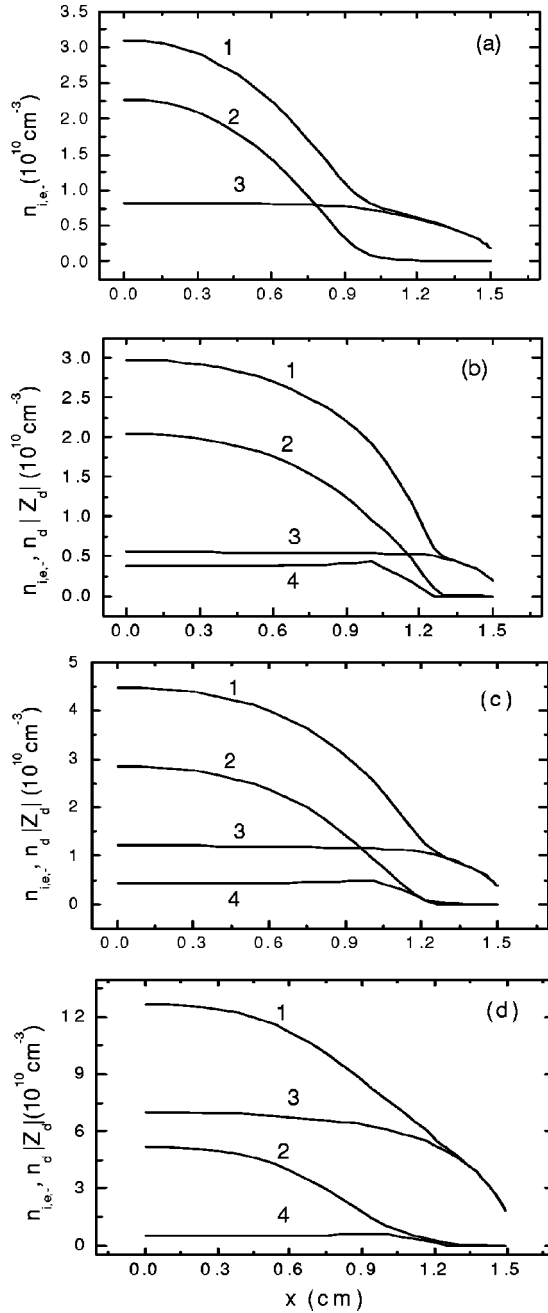


FIG. 2. Profiles of positive- (curve 1) and negative- (curve 2) ion densities, electron density (curve 3), and $n_d|Z_d|$ (curve 4) in a 100-mTorr discharge sustained plasma slab 3 cm thick. The value of the recombination coefficient is $K_{\text{rec}} = 2 \times 10^{-7} \text{ cm}^3/\text{s}$. Part (a) corresponds to the pristine plasma (no dust) at 0.12 W/cm^2 input power. Parts (b)–(d) are for a silane grain ($n_d = 2 \times 10^7 \text{ cm}^{-3}$, $a_d = 100 \text{ nm}$) containing plasma at input powers $P_{\text{in}} = 0.12, 0.24$, and 1.2 W/cm^2 , respectively.

Figures 2(a) and 2(b) show the profiles of n_e , n_i , n_- , and $n_d|Z_d|$ in a discharge sustained with $P_{\text{in}} = 0.12 \text{ W/cm}^2$. Some of the parameters are also given for the dust-free case. One can clearly see that in the latter case, the positive-ion density at the discharge midplane ($x=0$) is about four times larger than that of the electrons, whereas the electron density is almost uniform for $x \leq 1 \text{ cm}$. We note that the profiles in

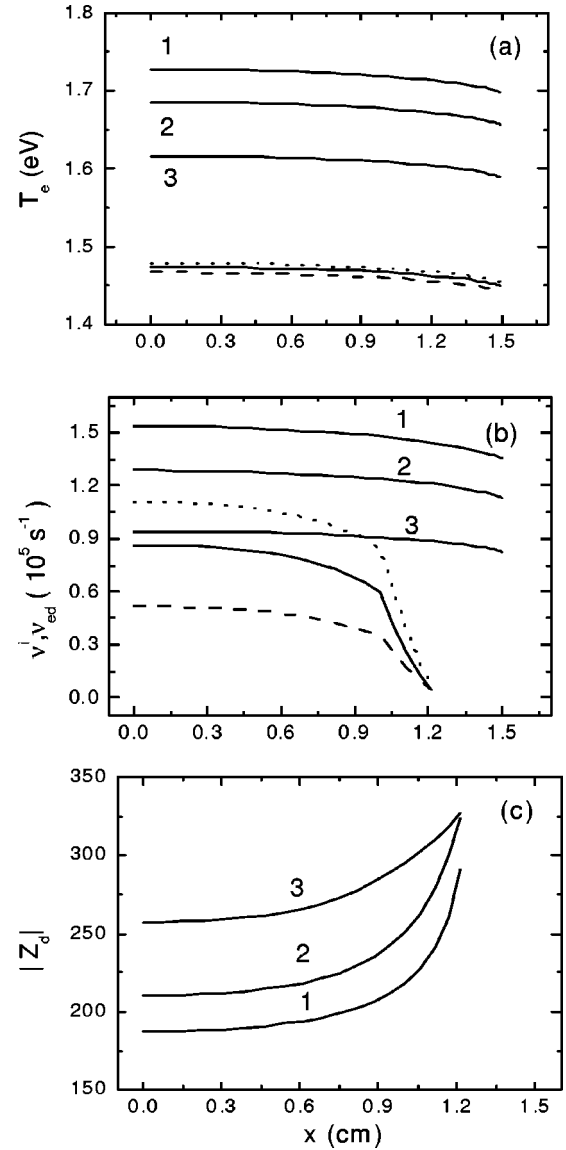


FIG. 3. Profiles of the electron temperature T_e (a), ionization rate ν^i (b), and absolute value of the dust charge (c) for different input powers: (curve 1) $P_{\text{in}} = 0.12 \text{ W/cm}^2$, (curve 2) $P_{\text{in}} = 0.24 \text{ W/cm}^2$, and (curve 3) $P_{\text{in}} = 1.2 \text{ W/cm}^2$. The unnumbered dotted, solid, and dashed curves in (a) and (b) correspond to T_e and ν_{ed} in the pristine plasma at input powers 0.12, 0.24, and 1.2 W/cm^2 , respectively. The other conditions are the same as in Fig. 2(b).

curves *a* of Fig. 1 are structurally similar to those in Figs. 10.2 and 10.3 of Ref. [3].

A comparison of Figs. 2(a) and 2(b) reveals the effect of dusts on the profiles of electron and ion densities. The electron density in the complex plasma is about 1.5 times smaller than in the dust-free plasma. Figure 2(a) also shows that the pristine plasma features larger gradients of the ion density in the region $x < 1 \text{ cm}$ as compared to that of the dust-containing discharge shown in Fig. 2(b). This difference in the plasma particle densities can be attributed to the effect of the dust grains on the electron temperature and the major reaction rates. Indeed, Fig. 3(a) clearly shows substantial en-

hancement of T_e as compared with that of the pristine plasma. The increment in the electron temperature can be attributed to the additional loss of electrons to the dusts. The complex plasma system self-organizes to compensate the losses incurred by the increased ionization and dissociation rates and electron temperature. At fixed input power levels, growth in T_e is accompanied by reduction of the electron density, a tendency also reported earlier [4,6,14].

The difference between the ion density profiles in the dusty and pristine plasmas can be attributed to the dependence of the rate of the electron capture by the dusts on the ratio n_i/n_e (18). One can show that ν_{ed} decreases towards the plasma wall [Fig. 3(b)]. Therefore, the losses of the positive ions on fine particles ($n_i\nu_{id} \approx n_e\nu_{ed}$) also decrease towards the discharge edges, thus making the ion density gradients in the discharge midplane smaller as compared to the pristine plasma case.

We now discuss the effect of the power absorbed by the plasma on the discharge equilibrium. The profiles of the particle densities for $P_{in}=0.24$ and 1.2 W/cm² are given in Figs. 2(c) and 2(d), respectively. From Figs. 2(b)–2(d) we see that the electron density increases almost linearly with P_{in} . We recall that this is also the case for most electropositive columns. On the other hand, the positive-ion density in the complex plasma rises significantly slower with power than that of n_e . Physically, although the ionization source of the positive ions is strengthened at higher power inputs, the relative role of the ion sink from the i^+-i^- recombination also increases. The latter impedes the linear growth of n_i with P_{in} , as common for electropositive plasmas.

The electron temperature profiles for different power levels are shown in Fig. 3(a). One can clearly see that in the dust-free case, represented by the dashed, solid, and dotted lines in Fig. 3(a), even an order-of-magnitude increase (from 0.12 to 1.2 W/cm²) of the input power only marginally changes the electron temperature. Thus, the power variation does not affect the dynamic balance between the ionization sources and diffusion or recombination losses of the plasma species determining the value of T_e when the dusts are absent. From the curves 1–3 in Fig. 3(a), we see that the presence of dusts significantly elevates the electron temperature, which however decreases with the input power. Lowering the input power decreases the electron density, and (at fixed n_d) also the proportion of electrons collected by the dusts relative to that absorbed by the discharge walls. That is, the dusts lead to a readjustment of the particle sources and sinks, which in turn affects the electron temperature.

In response to the input power increase, the complex plasma also tends to lower the ratio n_i/n_e and hence the rate $\nu_{ed} \propto n_i/n_e$ given by Eq. (18) of electron collection by the dusts, as seen in Fig. 3(b). One result is the increase of the dust charge with power, as seen in Fig. 3(c). This can be attributed to the accompanying increase of the electron and ion number densities.

VI. EFFECT OF THE NEUTRAL GAS PRESSURE

We also studied the effect of the working, or neutral, gas pressure p_0 on the discharge equilibrium. The profiles

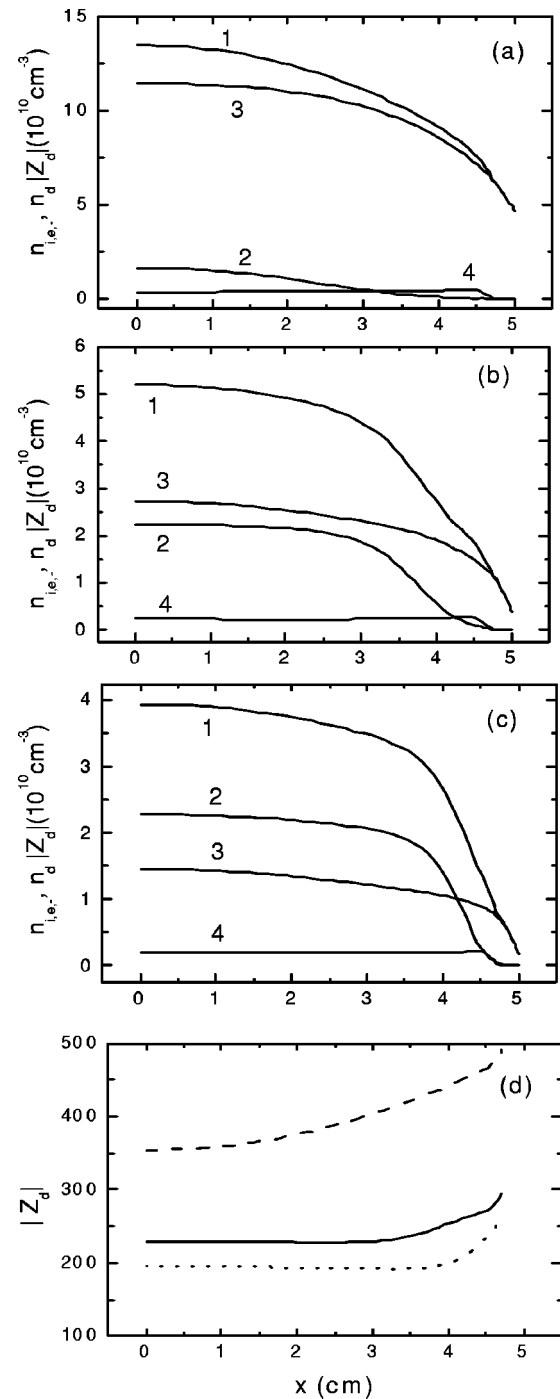


FIG. 4. Profiles of n_i (curve 1), n_- (curve 2), n_e (curve 3), and $n_d|Z_d|$ (curve 4) in a 10-cm-wide plasma slab containing silane at different gas pressures: (a) $p_0 = 10$ mTorr, (b) $p_0 = 100$ mTorr, and (c) $p_0 = 200$ mTorr. The dashed, solid, and dotted curves in (d) show $|Z_d|$ at 10, 100, and 200 mTorr gas pressures, respectively. The other conditions are the same as in Fig. 2(d).

($n_\alpha|Z_\alpha|$, where n_α and Z_α are the number density and charge of the species α) of the particle charge densities at different p_0 are shown in Figs. 4(a)–4(c). At the discharge midplane $x=0$, the electron temperature is 1.36, 1.44, and 2.03 eV for $p_0=200$, 100, and 10 mTorr, respectively. One can see that an increase of the gas pressure is accompanied by a drop of

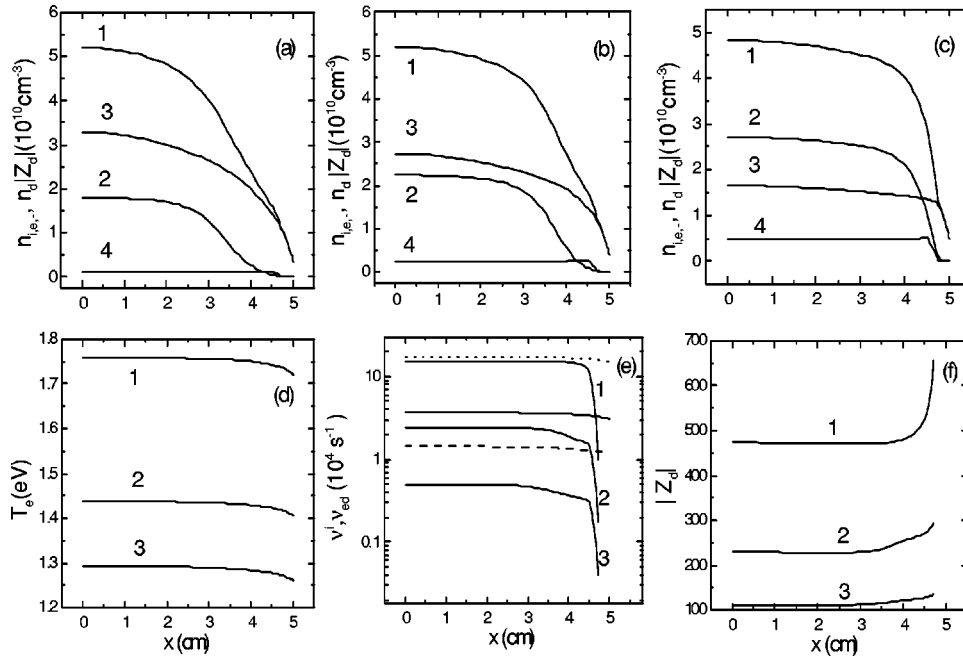


FIG. 5. Profiles of n_i (curve 1), n_- (curve 2), n_e (curve 3), and $n_d|Z_d|$ (curve 4) at $p_0=100$ mTorr for different dust radii: (a) $a_d=50$ nm, (b) 100 nm, and (c) 200 nm. The electron temperature (d), electron-dust collision rate (e), and the absolute value of the dust charge (f) are shown for $a_d=200$ nm (curve 1), 100 nm (curve 2), and 50 nm (curve 3). In (e) the dashed, solid, and dotted lines correspond to ν^i for $a_d=50$, 100, and 200 nm, respectively. The other conditions are the same as in Fig. 4.

the electron and ion densities as well as the electron temperature. The latter then results in a reduction of the dust charge, as seen in Fig. 4(d). It should be mentioned that a increase of gas pressure in argon electropositive plasmas is usually accompanied by a rise of the electron density and a drop of the electron temperature (see, e.g., Fig. 6 of Ref. [32]). Here, we observe exactly the opposite tendency in the electronegative silane plasma (Fig. 4). This behavior can be explained in terms of the fact that in the SiH_4 plasma, the threshold energies for nonelastic collisions are smaller than that in argon plasmas, and thus the nonelastic collision rates grow with the pressure. One can show that in the parameter range of interest, here the main power loss is due to vibrational excitation of the silane molecules. Owing to the low-energy threshold for the process (0.1–0.3 eV), the major collision rates appear to be less sensitive to the electron temperature variation with p_0 than to the accompanying changes in the density of the neutrals.

Thus, the main differences between the pristine and nanoparticle loaded plasmas are due to the collection of the plasma particles by the dusts. The enhanced electron temperature is required to sustain the extra electron loss via the enhanced ionization and dissociation. At fixed input power levels, the growth of T_e is accompanied by a decrease of n_e in the plasma bulk. On the other hand, both the electron and ion densities increase with the input power. However, the resulting enhanced i^+-i^- recombination results in smaller rates of increase of n_i (compared with that of n_e) with P_{in} . When the dust density is fixed, the dust proportion increases when the input power is decreased, resulting in a remarkably higher ionization and electron-dust collision rates, accompanied by higher T_e . Increase of P_{in} also leads to the growth of the particle number densities as well as the equilibrium nanoparticle charge. We emphasize that contrary to common tendencies in argon plasmas, the electron density declines with the gas pressure, which is attributed to a noticeable increase

of nonelastic electron losses (viz. via a vibration excitation of SiH_4 molecules) with p_0 .

VII. EFFECT OF THE DUSTS

In this section, the results on the effect of variation of number density, charge, and size of dust particles on the plasma properties are presented. The two different spatial distributions of n_d in Fig. 1 are considered.

A. Dust size

In Figs. 5(a)–5(c) the computed profiles of the plasma particle densities are shown for different dust radii 50, 100, and 200 nm, respectively. The formation of fine particles in this size range is quite typical for the developed rf silane based discharges. For example, 50-nm contaminant particles were observed in discharges of argon-silane gas mixtures about 12 sec after the plasma start-up [38]. Growth of 100 and 200 nm grains required about 40 and 80 sec (see Figs. 1 and 4 of Ref. [38]), respectively. At this stage, an increase in the dust size is predominantly due to the coagulation of smaller particles [6].

From Figs. 5(a)–5(c), one can see that the electron density decreases with the dust size, while the negative-ion density grows slightly. Likewise, the positive-ion density profile becomes flatter in the central area of the discharge. Presumably, the above changes can be attributed to variations of the electron temperature with the grain size, as depicted in Fig. 5(d). One can clearly see that the increase of the grain size is accompanied by a pronounced rise of T_e . Physically, larger surface area of the fine dusts supports higher loss of the plasma electrons that have to be reinstated by a higher rate of ionization at increased electron temperatures, as shown in Fig. 5(e). Furthermore, at higher T_e and fixed input power levels, the value of the electron collision integral J_e in Eq.

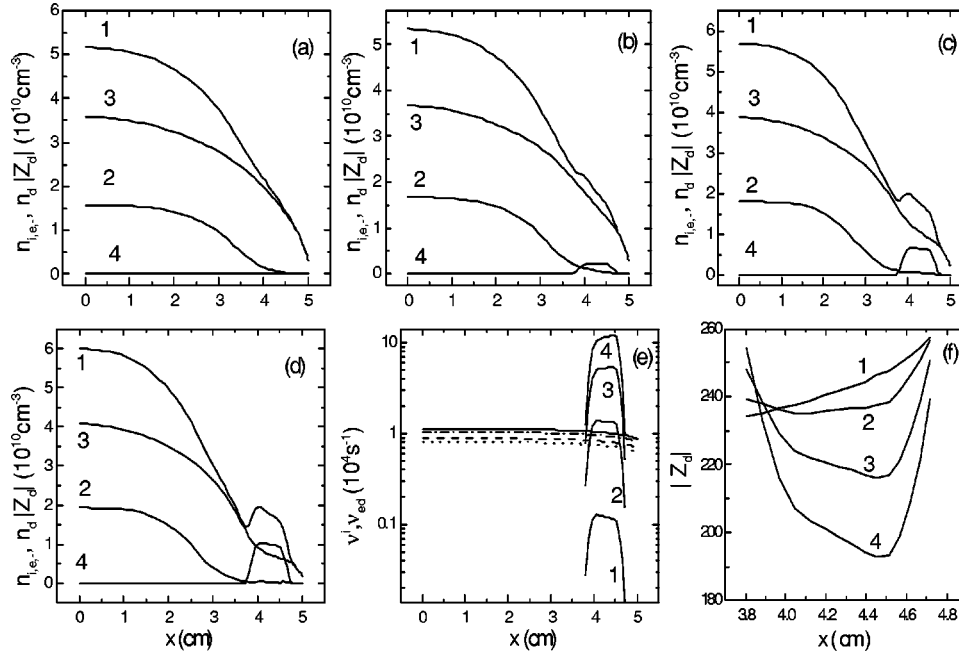


FIG. 6. Same as in Fig. 5 at $p_0 = 100$ mTorr. The dust density in the region $4 \text{ cm} < x < 4.5 \text{ cm}$ is 10^6 (a), 10^7 (b), 3×10^7 (c), and $5 \times 10^7 \text{ cm}^{-3}$ (d), respectively. Curves 1–4 in (e) for v_{ed} and (f) for $|Z_d|$, as well as the dotted, dashed, dash-dotted, and solid curves in (e) for v^i correspond to $n_d = 10^6 \text{ cm}^{-3}$, 10^7 cm^{-3} , $3 \times 10^7 \text{ cm}^{-3}$, and $5 \times 10^7 \text{ cm}^{-3}$, respectively. The other parameters are the same as in Fig. 4.

(9) also grows, so that the electron number density diminishes.

Furthermore, as the dust surface area increases, the electron-dust collision rate [see Fig. 5(e)] and the dust charge [Fig. 5(f)] also increase. Hence, change in the equilibrium dust charge also affects the densities of other plasma species [Figs. 5(a)–5(c)]. To preserve the overall charge neutrality of the plasma, the positive-ion density increases near the plasma edge where the variation of Z_d is more pronounced. Consequently, the shoulders of the positive-ion density profile become larger with the dust-size growth.

We note that the growth of the fine dusts also affects the negative-ion density, which increases slowly with a_d . This effect can be due to an increase of the electron attachment rate ν_{att} with T_e , which accompanies the particulate growth.

B. Dust density

We now turn our attention to the study of the effect of the fine particle density on the low-pressure discharge equilibrium. The study is carried out for a 100 mTorr silane plasma slab with $L = 10$ cm, sustained with input powers of $P_{in} = 1.2 \text{ W/cm}^2$. The recombination rate constant and dust radius are fixed at $2 \times 10^{-7} \text{ cm}^3/\text{s}$ and 100 nm, respectively. It is assumed that n_d in this case is uniform at $4 \text{ cm} < x < 4.5 \text{ cm}$ and linearly decreases to zero at $x = 3.75 \text{ cm}$ and $x = 4.25 \text{ cm}$ [curve *b* in Fig. 1].

The equilibrium profiles of the plasma species are shown in Figs. 6(a)–6(d) for dust densities of 10^6 , 10^7 , 3×10^7 , and $5 \times 10^7 \text{ cm}^{-3}$, respectively. It is clear that the profiles of n_j are sensitive to the dust concentration. For example, the electron density declines locally (in the dust-contaminated area) when n_d becomes larger. Specifically, $n_e = 3.3 \times 10^9$, 3.0×10^9 , 2.4×10^9 , and $1.8 \times 10^9 \text{ cm}^{-3}$ at $x = 5 \text{ cm}$ and the same n_d as in Figs. 6(a)–6(d). Apparently, the drop in the electron density is due to enhanced electron capture by the dusts. On the other hand, n_e decreases near the plasma edge,

so do the electron heat flux q_e at the boundary and the power lost at the discharge wall. This process is accompanied by a slight growth of the electron and ion densities in the central region of the plasma slab.

The electron temperature at the discharge midplane $x = 0$ rises from 1.217 to 1.258 eV when n_d is increased from 10^6 to $5 \times 10^7 \text{ cm}^{-3}$. The reason for this is the same as that in the preceding section, namely, the enlarged surface area for plasma particle collection. It is interesting to point out that the rate ν_{ed} of electron collection by the dusts increases with n_d and can be several times larger than the ionization rate, as can be seen in Fig. 6(e).

Interesting conclusions can also be drawn from the dependence of the equilibrium profiles of $|Z_d|$ on the concentration of the dusts, as displayed in Fig. 6(f). At smaller n_d , the dust charge grows monotonically along x direction. However, at larger dust densities, $|Z_d|$ drops for $x \leq 4.5 \text{ cm}$ and increases for $x > 4.5 \text{ cm}$. This tendency is quite similar to the dust charge distribution in the plasma sheath region [15]. Indeed, in the sheath and presheath regions featuring $n_i > n_e$ and high enough ion velocities, the charge on the dusts declines [15,27]. In our case the situation is quite similar near the discharge edge: the ion velocity is close to the Bohm velocity, whereas the ratio n_i/n_e is large enough to yield a decrease in $|Z_d|$.

We emphasize that the density, size, and spatial distribution of the fine dusts strongly affect the plasma parameters. As the grain size or concentration increases, the microscopic fluxes of the plasma species onto the dust surface also increase, enforcing a self-organization of the ionization source to reinstate the lost electron-ion pairs. The latter process requires an elevated electron temperature and smaller electron number densities. Furthermore, the equilibrium dust charge increases as the fine particle surface area grows. It is further accompanied by flattening of the positive-ion density profiles in the central areas of the plasma glow. If the dust cloud is

located near the plasma boundary, as in curve *b* in Fig. 1, the electron heat flux on the discharge walls decreases, thus increasing the densities of the plasma species in the central areas of the plasma reactor. Near the discharge edge, the difference between the electron and ion densities also increases with n_d .

VIII. EFFECT OF THE NEGATIVE IONS

The negative ions can also affect the equilibrium discharge state via a dynamic balance of the i^+-i^- recombination and electron attachment. Here, by varying the rate of the ion-ion recombination, we follow the changes in the electron temperature, electron and ion densities, and the dust charge.

The equilibrium spatial profiles of the plasma particle densities for $K_{\text{rec}}=10^{-8}$ cm³/s, and $K_{\text{rec}}=5.0\times 10^{-7}$ cm³/s are presented in Figs. 7(a) and 7(b), respectively. The relevant data for $K_{\text{rec}}=2\times 10^{-7}$ cm³/s and the same conditions as in Fig. 7(a) can be found in Fig. 5(b). One can clearly see that the ion density diminishes with an increase of the i^+-i^- recombination rate. It is further observed that ion-ion recombination affects mainly the loss of the plasma ions. It does not directly affect the balance of the electrons since the analogous terms are not present in the electron balance equation (1). Nevertheless, the electron density diminishes slightly when the recombination rate decreases. This effect is likely to be due to the indirect effect of ion-ion recombination on the electron temperature and collision processes.

The ion densities are strongly affected by the i^+-i^- recombination rate, and the ratio n_i/n_e becomes larger when K_{rec} decreases. We see from Eq. (18) that $v_{ed}\propto n_i/n_e$, so that the rate of the electron or ion capture by the dusts is smaller when the ion-ion recombination is stronger, as is shown in Fig. 7(c). Therefore, for a smaller ion-ion recombination coefficient, the fluxes of the plasma species onto the dusts are larger. Consequently, the electron temperature declines with K_{rec} . Specifically, $T_e=1.6$ and 1.42 eV for $K_{\text{rec}}=10^{-8}$ cm³/s and 5.0×10^{-7} cm³/s, respectively. Similar to the results of the previous sections, the growth of the electron temperature is accompanied by a small decrease of n_e .

From Fig. 7(d) one can see that the dust charge is larger when the recombination rate is higher. Indeed, the electron density declines and the positive-ion density grows when K_{rec} decreases. Apparently, this results in a change of the ratio n_i/n_e that controls rate (18) of electron collection by the dusts. Furthermore, at larger ratio n_i/n_e , condition (8) for dust charge equilibrium can be satisfied for smaller negative dust charges.

Thus, positive-ion–negative-ion recombination does affect the equilibrium profiles of the ion densities. The ion densities drop when the recombination process intensifies. As the corresponding rate K_{rec} increases, n_i/n_e and v_{ed} decrease. Hence, the negative dust charge grows to maintain the equilibrium plasma flux balance (on the dust grains) that is distorted by a rise of the electron number. Finally, when K_{rec} decreases, the electron temperature grows slightly to balance the enhanced electron loss onto the dust grains.

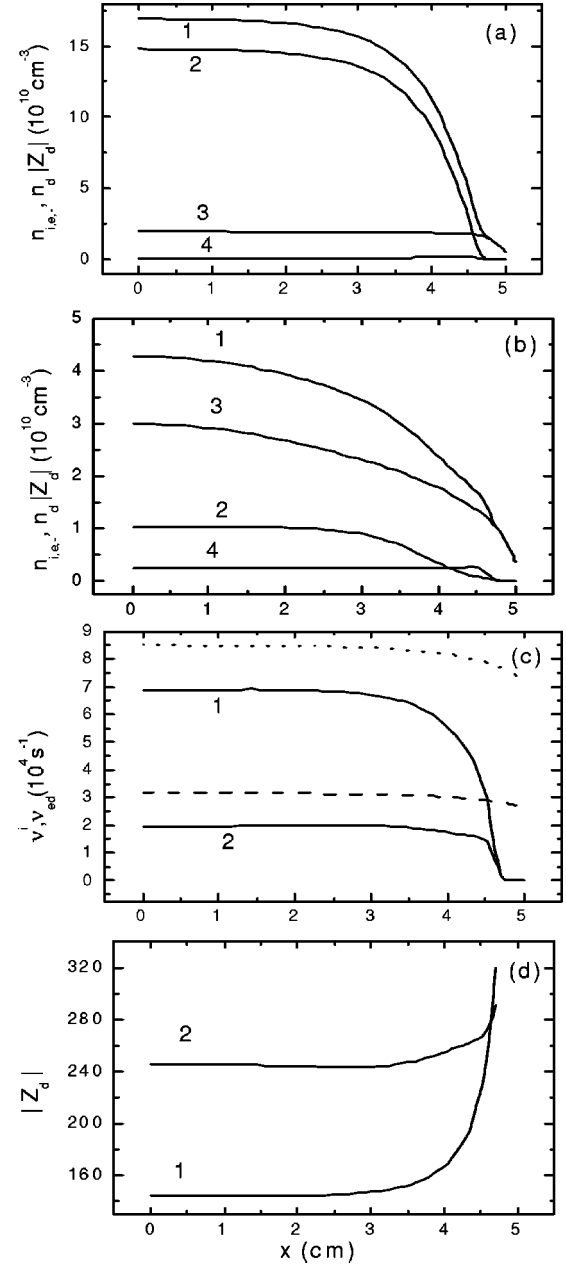


FIG. 7. Same as in Fig. 6, but for $a_d=100$ nm and different values of the recombination coefficient: $K_{\text{rec}}=10^{-8}$ cm³/s (a), and $K_{\text{rec}}=5\times 10^{-7}$ cm³/s (b). Curves 1 and 2 in (c) for v_{ed} and (d) for $|Z_d|$, as well as the dotted and dashed lines in (c) for v^i , are for $K_{\text{rec}}=10^{-8}$ and 5×10^{-7} cm³/s, respectively. The other conditions are the same as in Fig. 5.

IX. DISCUSSION

The model for low-pressure electronegative complex plasmas introduced here allows one to predict the equilibrium profiles of the electron temperature, the electron and ion number densities, as well as the dust charge. We emphasize that most of the existing models of dust-contaminated discharges are limited to studies of the effect of the charged dusts on the averaged, or global, parameters of the plasma (see, e.g., Refs. [6,17]), whereas our model also yields the spatial profiles of the major parameters.

We now discuss in more detail the limitations and implications of some of the assumptions made in our model. First, the size and spatial profiles of the fine dusts have been taken as external parameters in the numerical evaluations. In reality, the number density and size of the grains strongly depend on the neutral gas pressure, temperature, as well as the discharge volume. To predict the evolution of the particulate size and concentration, a much more detailed study of the dust nucleation or agglomeration is required [5,17]. However, self-consistent accounting of these complex processes will certainly significantly complicate the simple discharge model. Thus, in our calculations we have made no attempt to correlate the dust density and size. Instead, we have considered two specific dust particle profiles (Fig. 1) typical to laboratory experiments of complex plasmas. The fairly uniform profile of n_d [Fig. 1(a)] is relevant to dust growth in the entire reactor as is the case for the rf SiH_4 and $\text{SiH}_4 + \text{Ar/SiH}_4 + \text{H}_2$ plasmas [4,6]. This distribution is also applicable to experiments where the particles are injected externally [39]. The second case, with the dusts located at the plasma periphery [curve b in Fig. 1], is representative of dusts created in certain chemically active processing plasmas [34] and in the diffused regions of low-pressure rf discharges [40].

To some extent, the results of Secs. V–VII can be relevant in laboratory experiments on self-organized dust voids [41], where the dusts grown or injected into the plasma diffuse to the near-electrode areas. However, our 1D model is still short of reflecting the major features involving dust voids, such as asymmetry (due to intense positive ion fluxes to the electrodes), sharp boundaries of the void, nonuniformity of the plasma, etc. [41,42]. For simplicity, motion of the dust cloud boundary, motion of the relatively heavy dusts, as well as other dynamic processes in the plasma sheath have been precluded in this study. Furthermore, the boundaries of a dust cloud can act as virtual electrodes and promote formation of non-neutral layers (sheaths) in front of them [42]. Such layers can introduce substantial nonuniformity and destroy charge neutrality in regions adjacent to the dust cloud. A proper accounting for such processes would certainly improve the self-consistency of the model.

We note that accounting of electron collisional energy loss to the dusts would lead to new power-loss channels for the heating, excitation, and ionization of dust particles. However, the density of the dusts is typically small as compared to that of the neutrals. Besides, for the parameter values in our numerics, the total dust surface area is much smaller than the discharge wall surface area. The maximum dust density and radius considered are $5 \times 10^7 \text{ cm}^{-3}$ and 200 nm, respectively. Thus, in a parallel-plate discharge with $L = 10 \text{ cm}$, the combined total dust surface area of 0.6 cm^2 is still only a fraction of the electrode surface area of 2 cm^2 . Therefore, the electron energy loss to the dust grains is less important than that due to the electron-neutral collisions.

Our study has been carried out for steady state conditions assuming that the dusts are fixed. In most real silane rf discharges, this is not the case [4,5]. Nevertheless, the dust growth is a slow process in comparison with the diffusion and collision processes in such plasmas. For example,

$\approx 5 \text{ sec}$ are required for an increase of the dust size from 50 nm to 60 nm [16]. Therefore, dust growth can usually be treated in a quasi-stationary manner in discharge modelings.

Relatively large (exceeding a few ten nanometer in radius) dusts have been considered here. Such a size falls within the validity of the OML theory [26]. An extension of our model to the nanometer ($\sim 1\text{--}10 \text{ nm}$) domain would require substantial upgrading of the existing dust-charging theories to properly account for the size-dependent electron confinement and other effects.

In spite of the above limitations, the model used here is relatively simple, and accounts for the major particle sources and sinks in typical electronegative complex plasma systems. It also allows one to predict the local spatial profiles of the main plasma parameters for given characteristics of the dusts in the ionized gas phase.

X. APPLICATIONS

We now discuss the application of our model and results. First of them is for the removal or suppression of growth of the nanometer or micrometer-sized contaminants in plasma reactors. Our results show that one can control the number density and reactivity of the anion radical precursors of dust growth, such as SiH_3^- [4,5]. By decreasing the density of the SiH_3^- radicals, one can suppress the initial nucleation of the particulates or protoparticles that lead to the dust growth. On the other hand, most of the reaction rates are very sensitive to the electron temperature, which can also be controlled, for example, to enable low- T_e film growth [10]. The results here transparently reveal the domains of the main discharge and plasma parameters that allow one to minimize the number density of SiH_3^- radicals as well as to keep the electron temperature reasonably low. In particular, an increase of the electron and ion densities with the input power results in a drop in the density of negative ions relative to n_e and n_i (Fig. 2). The electron temperature also declines with power [Fig. 3(a)]. Alternatively, by decreasing the working gas pressure, one can also lower the relative negative-ion density (Fig. 4), although with somewhat elevated T_e . Alternatively, an increase of the dust size is accompanied by a rise of T_e as well as n_- (Fig. 5). Thus, both the negative-ion precursor radicals and the electron temperature can be controlled by the input power together with working gas pressure, as well as by an additional injection of dusts into the plasma reactor.

Apart from many deleterious implications, dust loaded plasmas have recently proved to be instrumental in several, advanced, particle based technologies [43]. For example, processing with externally injected nanoparticles can yield novel objects such as tailored surface structures with specific properties [4]. Moreover, dust particles with specific properties are directly useful in many applications, such as in modern printing machines and optical devices [44].

It is worth noting that higher-density low-pressure discharges (with lower density of the negative-ion precursors) are more suitable than low- n_e plasma glows for the production of complex plasmas with relatively low dust concentration. Thus, one can expect that ICP sources will feature (as a

result of homogeneous nucleation [5]) lower gas-phase grown dust contamination as compared with the CCPs. Indeed, in general, the ICPs feature higher electron densities and lower electron temperatures [45] as compared to the CCPs.

XI. CONCLUSION

A model for electronegative plasmas containing charged dust or colloidal grains has been used. Numerical solutions based on the model demonstrate how a low-pressure diffusion equilibrium of the complex electronegative plasma system is dynamically sustained through plasma particle sources and sinks. The spatial profiles of the electron, positive- and negative-ion densities, electron temperature, and equilibrium dust charge have been obtained for different values of the external and internal parameters. Variations of the input power, working gas pressure, fine particle size, and density result in remarkable changes in the electron temperature and some of the major reaction rates, which can dynamically affect the equilibrium states of the low-pressure discharge. In

particular, one can selectively control the parameter ranges in order to minimize the negative-ion precursors for dust growth and obtain the appropriate electron temperature. Thus, our results can be used as a guide in optimizing the discharge parameters for specific applications.

The present study can be considered as a first step in the study of dynamic self-organization in complex plasmas containing negative ions and nanometer-sized dust grains. An extension of our model to include the actual time-dependent reactive chemistries and evolution of the dust particulates would be highly desirable.

ACKNOWLEDGMENTS

This work was supported in part by the Agency for Science, Technology, and Research of Singapore (Project No. 012 101 00247), the Australian Research Council, and NATO (Grant No. PST.CLG.978083). Fruitful discussions with N. F. Cramer, D. McKenzie, and V. Ligatchev are gratefully acknowledged.

-
- [1] *ULSI Technology*, edited by C.Y. Chang and S.M. Sze (McGraw-Hill, New York, 1996).
 - [2] *Plasma Etching: An Introduction*, edited by D.M. Manos and D.L. Flamm (Academic, New York, 1989).
 - [3] M.A. Lieberman and A.J. Lichtenberg, *Principles of Plasma Discharges and Materials Processing* (Wiley, New York, 1994).
 - [4] *Dusty Plasmas: Physics, Chemistry, and Technological Impacts in Plasma Processing*, edited by A. Bouchoule (Wiley, New York, 1999).
 - [5] Ch. Hollenstein, *Plasma Phys. Controlled Fusion* **42**, R93 (2000).
 - [6] A.A. Fridman, L. Boufendi, T. Hbid, B.V. Potapkin, and A. Bouchoule, *J. Appl. Phys.* **79**, 1303 (1996).
 - [7] A. Hadjadj, L. Boufendi, S. Huet, S. Schelz, P. Roca i Cabarrocas, H. Estrade-Szwarczkopf, and B. Rousseau, *J. Vac. Sci. Technol. A* **18**, 529 (2000).
 - [8] R. Martins, H. Aguas, I. Ferreira, V. Silva, A. Cabrita, and E. Fortunato, *Thin Solid Films* **383**, 165 (2001).
 - [9] M. Meaudre, R. Meaudre, R. Butte, S. Vignoli, C. Longeaud, J.P. Kleider, and P. Roca i Cabarrocas, *J. Appl. Phys.* **86**, 946 (1999).
 - [10] M. Takai, T. Nishimoto, M. Kondo, and A. Matsuda, *Appl. Phys. Lett.* **77**, 2828 (2000).
 - [11] S.J. Choi and M.J. Kushner, *J. Appl. Phys.* **74**, 853 (1993).
 - [12] Y. Hori, K.N. Ostrikov, H. Toyoda, and H. Sugai, in *Proceedings of XXV International Conference Phenomeneal Ionic Gases, Nagoya, Japan, 2001*, edited by T. Goto (Nagoya University Press, Nagoya, 2001).
 - [13] K.N. Ostrikov, M.Y. Yu, and H. Sugai, *J. Appl. Phys.* **86**, 2425 (1999).
 - [14] K.N. Ostrikov and M.Y. Yu, *J. Phys. D* **32**, 1650 (1999).
 - [15] S.V. Vladimirov and N.F. Cramer, *Phys. Rev. E* **62**, 2754 (2000).
 - [16] A. Bouchoule and L. Boufendi, *Plasma Sources Sci. Technol.* **2**, 204 (1993).
 - [17] U. Kortshagen and U. Bhandarkar, *Phys. Rev. E* **60**, 887 (1999).
 - [18] H.C. Kim and V.I. Manousiouthakis, *J. Appl. Phys.* **89**, 34 (2001).
 - [19] V.N. Tsytovich, *Usp. Fiz. Nauk* **40**, 53 (1997) [*Phys. Usp.* **40**, 53 (1997)], and references therein.
 - [20] K.N. Ostrikov, S.V. Vladimirov, M.Y. Yu, and G.E. Morfill, *Phys. Rev. E* **61**, 4315 (2000).
 - [21] K.N. Ostrikov, S.V. Vladimirov, M.Y. Yu, and G.E. Morfill, *Phys. Plasmas* **7**, 461 (2000).
 - [22] S.V. Vladimirov, K. Ostrikov, M.Y. Yu, and G.E. Morfill, *Phys. Rev. E* **67**, 036406 (2003).
 - [23] S. Stoykov, C. Eggs, and U. Kortshagen, *J. Phys. D: Appl. Phys.* **34**, 2160 (2001).
 - [24] K. Takahashi and K. Tachibana, *J. Appl. Phys.* **89**, 893 (2001); *J. Vac. Sci. Technol. A* **19**, 2055 (2001).
 - [25] V.E. Golant, A.P. Zhilinskii, and I.E. Sakharov, *Fundamentals of Plasma Physics* (Wiley, New York, 1980).
 - [26] M.S. Barnes, J.H. Keller, J.C. Forster, J.A. O'Neill, and D.K. Coultas, *Phys. Rev. Lett.* **68**, 313 (1992).
 - [27] K.N. Ostrikov, S. Kumar, and H. Sugai, *Phys. Plasmas* **8**, 3490 (2001).
 - [28] I.B. Denysenko, A.V. Gapon, N.A. Azarenkov, K.N. Ostrikov, and M.Y. Yu, *Phys. Rev. E* **65**, 046419 (2002).
 - [29] K.N. Ostrikov, I.B. Denysenko, E.L. Tsakadze, S. Xu, and R.G. Storer, *J. Appl. Phys.* **92**, 4935 (2002).
 - [30] S.V. Vladimirov and V.N. Tsytovich, *Phys. Rev. E* **58**, 2415 (1998).
 - [31] S.V. Vladimirov, *Phys. Rev. E* **50**, 1422 (1994).
 - [32] N.A. Azarenkov, I.B. Denysenko, A.V. Gapon, and T.W. Johnston, *Phys. Plasmas* **8**, 1467 (2001).
 - [33] M. Yan and W.J. Goedheer, *Plasma Sources Sci. Technol.* **8**, 349 (1999).

- [34] A. Garscadden, B.N. Ganguly, P.D. Haaland, and J. Williams, *Plasma Sources Sci. Technol.* **3**, 239 (1994).
- [35] M. Kurachi and Y. Nakamura, *J. Phys. D: Appl. Phys.* **22**, 107 (1989).
- [36] M.J. Kushner, *J. Appl. Phys.* **63**, 2532 (1988).
- [37] J.P. Boeuf and Ph. Belenguer, *J. Appl. Phys.* **71**, 4751 (1992).
- [38] L. Boufendi and A. Bouchoule, *Plasma Sources Sci. Technol.* **3**, 262 (1994).
- [39] K. Tachibana and Y. Hayashi, *Pure Appl. Chem.* **68**, 1107 (1996).
- [40] N. Hayashi, *Phys. Plasmas* **8**, 3051 (2001).
- [41] D. Samsonov and J. Goree, *Phys. Rev. E* **59**, 1047 (1999).
- [42] J. Goree, G.E. Morfill, V.N. Tsytovich, and S.V. Vladimirov, *Phys. Rev. E* **59**, 7055 (1999).
- [43] E. Stoffels, W.W. Stoffels, H. Kersten, G.H.P.M. Swinkels, and G.M.W. Kroesen, *Phys. Scr., T* **89**, 168 (2001).
- [44] H. Kersten, P. Schmetz, and G.M.W. Kroesen, *Surf. Coat. Technol.* **108**, 507 (1998).
- [45] S. Xu, K.N. Ostrikov, Y. Li, E.L. Tsakadze, and I.R. Jones, *Phys. Plasmas* **8**, 2549 (2001).